ARMA 21–2047

Investigation of Fracture Process Zone in Barre Granite under Mode II Loading

Garg, Prasoon
Colorado School of Mines, Golden, Colorado, USA
Hedayat, Ahmadreza
Colorado School of Mines, Golden, Colorado, USA
Griffiths, D.V.
Colorado School of Mines, Golden, Colorado, USA

ABSTRACT: Fracturing in brittle rocks exhibits a significant nonlinear region surrounding the crack tip called the fracture process zone (FPZ). In this study, the evolution of the FPZ under pure mode II loading using notched deep beam under three-point loading was investigated. The experimental setup included the simultaneous monitoring of surface deformation using the two-dimensional digital image correlation technique to characterize various crack characteristics such as its type and FPZ evolution in Barre granite specimens. Both displacement and strain approaches of the two-dimensional digital image correlation were used to identify the mode of fracture under pure mode II loading. Both approaches showed that the crack initiation occur under mode I despite the pure mode II loading at the notch tip. The displacement approach was used for characterizing the evolution of the FPZ which analyzed the crack tip opening displacement and crack tip sliding displacement to identify the transition between the three stages of FPZ evolution, namely, (a) elastic stage, (b) formation of the FPZ, and (c) the macro-crack initiation. The results showed that the evolution of the FPZ of mode I fracture under pure mode II loading is similar to cases of pure mode I loading of the same rock.

1. INTRODUCTION

The fracturing in rocks and other quasi-brittle such as concrete is often characterized by a significant inelastic region surrounding the crack tips (Labuz et al., 1987). The inelastic deformation occurs due to the formation of a micro-cracking zone, also known as the fracture process zone (FPZ), which has a significant impact on the overall failure of laboratory-scale rock specimens, as its size is often comparable to pre-existing cracks (Ghamgosar and Erarslan, 2016).

For mixed-mode I/II and mode II fractures, most studies (Aliha et al., 2006; Aliha and Ayatollahi, 2014; Luo et al., 2017; Mirsayar et al., 2018) still assumes the linear elastic fracture mechanics (LEFM) thereby neglect the influence of the FPZ. However, recent studies such as Lin et al. (2014, 2020) and Xing et al. (2020) have found a significantly larger size of the FPZ (compared to LEFM based criterion) under both mixed-mode I/II and mode II loading conditions for various quasi-brittle materials such as cement mortar and Berea sandstone. Based on the concept of the LEFM, many studies (Aliha et al., 2006; Ayatollahi and Sistaninia, 2011; Mirsayar et al., 2018) also assume that pure mode II loading is equivalent to pure mode II fracture. However, some studies (Ji et al., 2016; Lin et al., 2020, 2019; Liu et al., 2018) have found that pure mode II loading doesn't necessarily lead to pure mode II fracture and suggested a distinction between the applied mode of loading and the fracture mode. For instance, Ji et al. (2016) compared two disc-type testing configurations, namely semi-circular disk specimens under three-point bending (SCB) and centrally cracked Brazilian disc (CCBD), and only found mode I or mixed-mode I-II fractures in these specimen geometries, despite the fact that the specimens were subjected to the pure mode II loading condition. Similarly, Lin et al. (2020), based on the FPZ development in the different testing configurations used for mode II fracture toughness, found that the pure mode II cracks were difficult to create without the elimination of the tensile stresses at the crack tip by applying the confining stresses.

In all of the aforementioned studies, a fundamental question that remains unanswered is "how mode II loading influences the development of the FPZ and the fracture mode." To answer this question, a detailed analysis of the FPZ development under pure mode II loading is needed especially based on local stress or strain field inside the FPZ. Optical techniques such as digital image correlation (DIC) can be a vital tool to characterize the FPZ development as DIC provides direct measurements of the displacement and strain fields inside the FPZ. In DIC, the surface features are tracked by comparing the digital images of a specimen surface during the experiment with respect to a reference image (Sutton et al., 2009) in order to obtain full-field surface

deformation. Because of its simple setup and accurate measurements, DIC has gained attention in experimental fracture mechanics (Aliabadian et al., 2019; Garg et al., 2019; Hedayat et al., 2014; Miao et al., 2018; Sharafisafa et al., 2018; Shirole et al., 2020b; Zhang et al., 2018).

In this study, the notch deep beam (NDB) configuration was used to characterize the FPZ development under pure mode II loading. The NDB configuration was selected due to its numerous advantages over other available geometries such as the cylindrical specimens, due to its ease of preparation and availability of multiple specimen configurations for pure mode II loading (Luo et al., 2017). Additionally, the NDB configuration provides a large ligament length depending on notch length, which facilitates the formation of fully developed FPZ from the notch tip without any boundary effects. The NDB specimens of Barre granite were loaded under three-point bending along with the simultaneous implementation of 2D-DIC to characterize the various crack characteristics such as the FPZ evolution and its crack type under pure mode II loading. The configuration corresponding to pure mode II loading was estimated using the LEFM based finite element analysis. The mode of fracture was determined based on both displacement and strain approaches of 2D-DIC. Additionally, the FPZ evolution under pure mode II loading was characterized using displacement approach of 2D-DIC based on the methodology developed by the authors (Garg et al., 2020a-b).

2. NDB CONFIGURATION FOR PURE MODE II LOADING

The NDB test configuration was selected in the current study due to its ability to achieve various loading conditions from pure mode I to pure mode II, just by changing the notch inclination. The NDB specimen is a prismatic beam with a notch inclined at an angle α with respect to the loading direction (Figure 1a), subjected to a symmetrical three-point bending with a span of $2d$. Based on the work of Lu et al. (2017), the stress intensity factors K_I and K_{II} for the NDB specimen under three-point bending can be defined as follows:

$$Y_I\left(\frac{a}{W},\frac{d}{W},\alpha\right) = \frac{K_I}{\sqrt{\pi a}}\frac{2WB}{P} \quad (1)$$

$$Y_{II}\left(\frac{a}{W},\frac{d}{W},\alpha\right) = \frac{K_{II}}{\sqrt{\pi a}}\frac{2WB}{P} \quad (2)$$

where P is the applied load, W is beam depth, B is the beam thickness, d is the half span, and Y_I and Y_{II} are the mode I and mode II non-dimensional geometrical factors, respectively. Both geometrical factors (Y_I and Y_{II}) depend on various parameters such as the span to depth ratio (d/W), the notch inclination angle (α), and notch length to depth ratio (a/W). The specimen is under pure mode I loading for the notch inclination (α) equal to zero, which eventually changes to pure mode II loading ($Y_I = 0$) at a specific angle (α) depending on the span to depth ratio (d/W) and notch length to depth ratio (a/W).

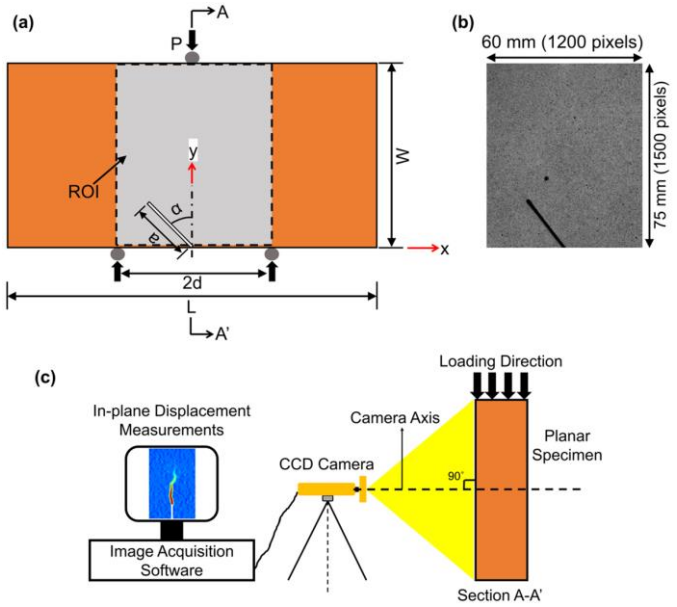

Figure 1. (a) Three-point bending test on NDB specimen along with the field of view for DIC analysis, (b) Image of the speckle pattern obtained on specimen NDB-1, and (c) The schematic of the experimental setup used for a three-point bending test (figure not in scale).

In this study, two geometrical factors were estimated using the commercial general-purpose finite element package ABAQUS. Figure 2 shows the finite element mesh of the three-point bend test on NDB specimen under plane strain conditions. A singular 6-node quadratic plane strain triangle element type (CPE6) was used for the first ring of elements around the crack tip, and an 8-node biquadratic plane strain quadrilateral element type (CPE8) was employed for the other elements. To smoothen the curves of the J- integral paths, 20 rings of quadrilateral elements (40 elements for each ring) around the crack tip were meshed using the sweep technique (Figure 2). The modeled specimen in the current study had the same nominal dimensions as the experiments with a line crack representing the inclined notch (Figure 1a and 2). To model three-point bending, a displacement rate of 0.1 mm/step (1step =1sec) was applied at the top of the beam. The material behavior was assumed to be linearly elastic with Young's modulus (E_t) of 28 GPa and Poisson's ratio (ν) of 0.16 to represents elastic properties of Barre granite based on the study Goldsmith et al. (1976). In the numerical models, the notch inclination angle (α) was varied from 0º to 60º. The beam has length to depth ratio (L/W) of 0.5 along with notch length (a) of 26 mm, which is kept constant in all the models. Two cases of span to depth ratio (d/W) of 0.4 and 0.5 were simulated to estimate the notch inclination angle (α)

corresponding to pure mode II loading condition. Figures 3a-b show the variations in the dimensionless factors Y_I and Y_{II} for both span to depth ratio (d/W) in the modeled NDB specimens. In both cases, pure mode I (opening mode) was obtained when the notch inclination angle (α) was zero. As the notch inclination angle (α) increased, Y_I decreased, whereas Y_{II} initially increased and then decreased. The pure mode II loading (i.e.,$Y_I = 0$) was achieved at angles of 38.1° and 56.7° for span to depth ratios (d/W) of 0.4 and 0.5, respectively (Table 1).

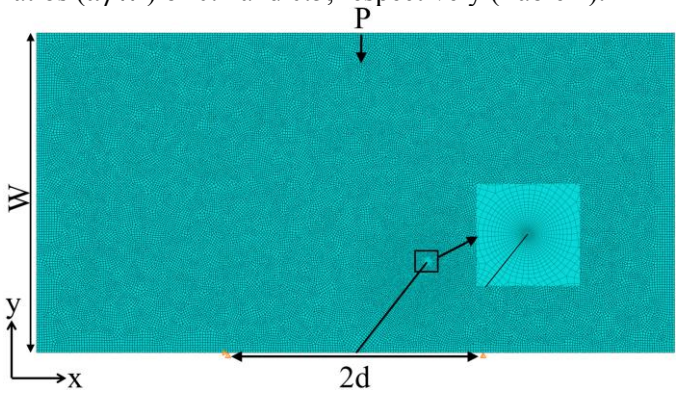

Figure 2. Finite element mesh used for estimation of geometrical factors in NDB specimens.

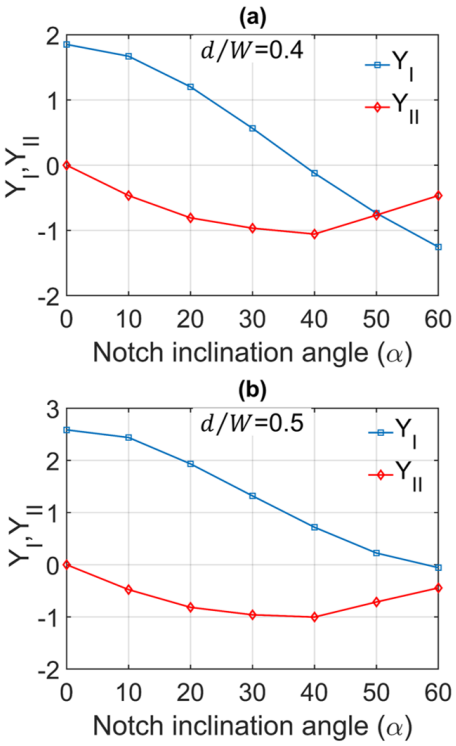

Figure 3. Variations of Y_I and Y_{II} for the modeled NDB specimens for a) d/W =0.4 and b) d/W =0.5.

3. EXPERIMENTAL DESIGN

3.1 Specimen Preparation

This study characterizes the fracture processes in Barre granite specimens under pure mode II loading. Barre granite is among the most extensively studied rocks, typically formed in the Devonian New Hampshire pluton series of Burlington, Vermont (USA) (Dai and Xia, 2010; Goldsmith et al., 1976; Saadat and Taheri, 2019). It has a consistent mineral composition with feldspar (65% by volume), quartz (25% by volume), and biotite (9% by volume) as its primary constituents (Iqbal and Mohanty, 2006; Nasseri et al., 2010). A large block of Barre granite was used to prepare prismatic specimens with dimensions of length L=150 mm, height H=75 mm, and thickness B=25 mm (Figures 1a). All the surfaces of each specimen were then grounded to ensure the desired level of dimension. A center notch of 1.02 mm aperture was created by the Colorado WaterJet Company. The length of the notch (a) is 26 mm (Figure 1a). The specimens with support span ratio (d/W) of 0.4, 0.5 were tested with a notch inclination angle of 38.1° and 56.7°, respectively, (Table 1) to represent pure mode II loading (Figure 1a).

Table 1: Notch inclination angle corresponding to pure mode II loading on NDB specimens.

Specimen #	NDB-1	NDB-2
notch inclination angle α (deg.)	38.1°	56.7°
span to depth ratio (d/W)	0.4	0.5

3.2 Experimental Setup and Testing

The three-point bending tests were conducted on the NDB specimens of Barre granite using an MTS servo-controlled loading machine. The specimens were loaded at the constant axial displacement rate of 0.1 µm/sec. Additionally, the crack mouth opening displacement (CMOD) was measured by an extensometer called a clip-on gauge bonded to the beam's bottom surface. The extensometer measured the displacement between two clips across the gauge length of 12 mm.

A 2D-DIC system mainly consists of a CCD (Charged-coupled device) camera placed perpendicular to the specimen surface (Figure 1c) along with steady white sources and an image acquisition system. In this study, the CCD camera with 2448 by 2048 square pixels capability was used in combination with a Fujinon lens of 17.5 mm focal length (Model CF35HA-1). The Pylon Viewer software was used to control the camera and capture the images of ROI of a small area of 60×75 mm^2 around the beam center (Figure 1a-b). During each three-point bending test, digital images of the speckled surface were captured at the rate of 10 frames/sec until total failure of the specimen. The images obtained were analyzed using the Correlated Solutions software (VIC-2D) to obtain surface deformation and strain fields inside the ROI of each specimen which required three input parameters, namely (a) subset size, (b) step size, and (c) filter size. The optimum values of each parameter is vital for a proper characterization of localized strain inside the FPZ. In the current study, the subset size of 31 pixels and the step size

of 5 pixels were used, as suggested by the author's earlier study (Garg et al. (2020b)). The parameters selected ensured that high strain values inside the FPZ were measured with reasonable accuracy without distorting its size (for more details, please refer to Garg et al., 2020b).

4. EXPERIMENTAL RESULTS

4.1 Fracture mode characterization using the displacement approach

This section presents the methodology for characterizing the fracture mode in Barre granite specimens using the displacement approach of 2D-DIC. Based on the LEFM, the fracture mode is defined based on the displacement profiles along the crack faces. For instance, a mode I crack (tensile crack) only has normal displacements along its faces (i.e., opening displacements), while a mode II crack (shear crack) has displacements parallel to the crack faces (i.e., sliding displacements). Similarly, mixed-mode I/II crack has both opening and sliding displacements along its faces. Several studies, such as Lin et al. (2014) and Ji et al. (2016) have shown that the characteristics of the fracture, such as its mode and location, can be identified by analyzing the displacement field inside the FPZ. Therefore, the 2D-DIC based displacement field inside FPZ can be used to determine the mode of fracture.

In this study, the full-field displacements at the peak load stage were analyzed to determine the mode of fracture. The peak load stage is used because it represents the stage just before the FPZ transition to macro-crack. The macro-crack initiation stage was identified based on the methodology developed by authors (see details in Garg et al., 2020a-b). Figure 4a-b shows the distribution of horizontal (U) and vertical displacement (V) fields at the peak load stage for specimen NDB-1, which has a notch inclination (α) of 38.1º (Table 1). The measured displacements were calculated based on the reference image at the beginning of the test and thus represent total displacements at the peak load stage. It is clearly shown in figure 4a-b that the FPZ (characterized by the merged displacement contours) has formed above the notch tip at an angle β from the notch plane resulting in the formation of a fracture 'kink' from the tip. This observation is consistent with other studies (Ji et al., 2016; Lin et al., (2019, 2020)) on the three-point tests of semi-circular disk specimens under pure mode II loading. These studies have attributed the formation of 'kink' to tensile stress concentration around the notch tip that consequently resulted in the mode I fracture despite the application of pure mode II loading at the notch tip. Figure 4a also shows a neutral axis at y = 48 mm in the horizontal displacement (U), which is distorted due to the presence of shear loading and formation of a displacement discontinuity above the notch tip. It is be noted that a small amount of rigid body motion has occurred in the specimen, which has resulted in a non-zero value of horizontal displacement along the neutral axis.

To determine the fracture mode, a local coordinate system (x_1, y_1) was established by rotating the global coordinate system (x, y) such that axis y_1 is along the direction of the FPZ (Figure 4a). Both horizontal and vertical displacements (U, V) were transformed into the local coordinate system to obtain the normal and tangential displacements field (U_1, V_1) along the FPZ as shown in Figure 4c-d. It is clear from Figure 4c that displacement discontinuity has formed in the contour of normal displacement (U_1) indicating the presence of the mode I component in the FPZ while in the case of tangential displacement (V_1), a continuous distribution is observed (Figure 4d) with no indication of the FPZ formation. This suggests that facture is unlikely to have a mode II component.

In order to quantify the displacements (both opening and sliding) inside the FPZ, two cross-sections parallel to the FPZ ($x_1 = \pm 2$ mm) were selected to represent its approximate boundary (Figure 4c-d). These cross-sections were chosen to ensure that the effect of measurement errors close to the crack plane (merged contours) can be avoided. Both normal and tangential displacements were calculated at various points along these two cross-sections, as shown in Figure 4e-f. It can be inferred from Figure 4e-f that the FPZ only has opening displacements and no (negligible) sliding displacements. Therefore, in specimen NDB-1, the FPZ will transition into a mode I fracture rather than mode II, which is further confirmed by the continuous distribution of the tangential displacement field (Figure 4d). Additionally, the opening displacement inside the FPZ is non-symmetric as the normal displacement with respect to the crack plane on the left side of the FPZ is more than on its right side (Figure 4e). Thus, the opening displacement at the notch tip with respect to the crack plane on the left side (27 μm) is around three times the opening displacement on the right side of the FPZ (9 μm) (Figure 4e) which can be attributed to the influence of shear loading at the notch tip. This observation is consistent with other studies such as Lin et al. (2019, 2020) on the three-point bending tests of Berea sandstone that have found a non-symmetric pattern of the normal displacement at the notch tip under pure mode II loading. Additionally, at the notch tip, crack opening displacement ($CTOD$) and crack sliding displacement ($CTSD$) is defined as relative opening and sliding displacement, respectively, between two cross-sections ($x_1 = \pm 2$ mm) (Figure 5e-f). Both parameters were used to characterize the FPZ evolution under pure mode II loading (section 4.3).

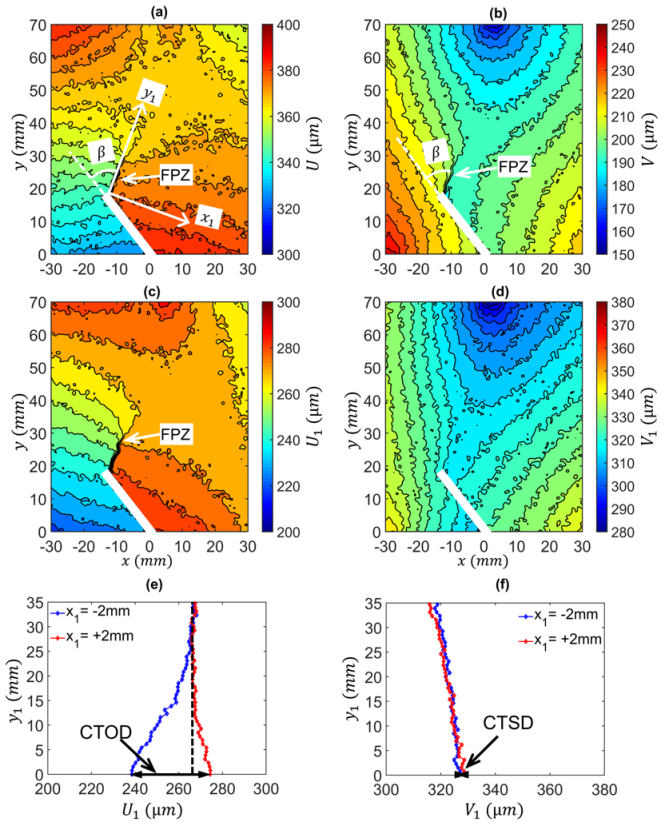

Figure 4. Specimen NDB-1, at peak load stage: Contours of (a) horizontal displacement field, (b) vertical displacement field, (c) normal displacement field, (d) tangential displacement field; Profiles of (e) normal displacement, (f) tangential displacement along two cross-sections of the FPZ. CTOD is crack tip opening displacement and CTSD is crack tip sliding displacement.

The displacement-based 2D-DIC analysis also shows the formation of a kinked mode I fracture in specimen NDB-2, which has a notch inclination (α) of 56.7º (Table 1). Figure 5a-d presents the distribution of displacements contour in both global and local coordinate systems at the peak load stage. It is clear from Figure 5a-b that the FPZ kinks from the notch tip at an angle of β from its plane. In addition, a tortuous crack path is observed in the specimen NDB-2 (Figure 5a-c), making it difficult to estimate the local coordinate system along the FPZ. Thus, the local coordinate system was transformed based on an average crack path from the notch tip as shown by axis-y_1 (Figure 5a) which also results in a distorted distribution of tangential displacement around the notch tip (Figure 5d). This leads to difficulties in determining the formation of the FPZ from tangential displacements because there are no clear observations of the displacement discontinuity (Figure 5d). Figure 5e-f shows a large opening displacement (~ 31 μm) along with a small amount of sliding displacement (~ 4 μm) at the notch tip of the specimen NDB-2 at the peak load stage. The non-zero value of the sliding displacement (~4 μm) can be again attributed to transformation based on the average crack path. A non-symmetric pattern of normal displacement inside the FPZ was also observed in specimen NDB-2, with its left side having the opening displacement (with respect to crack plane) around 2.5 times compared to the opening displacement on the right side of the FPZ (Figure 5e). Therefore, it can be concluded that the fracture initiation in specimens NDB-2 is due to mode I deformation based on the displacement approach of 2D-DIC.

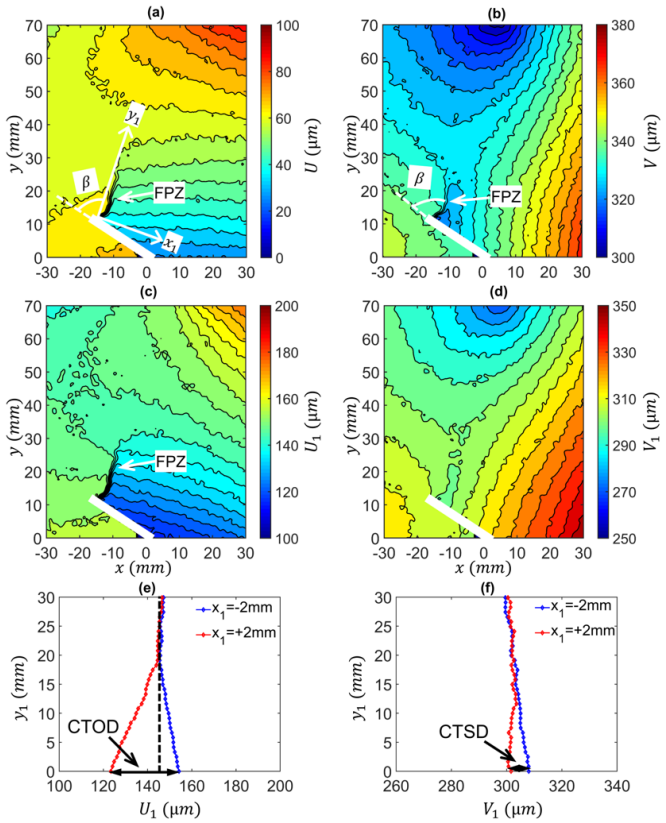

Figure 5. Specimen NDB-2, at peak load stage: Contours of (a) horizontal displacement field, (b) vertical displacement field, (c) normal displacement field, (d) tangential displacement field; Profiles of (e) normal displacement, (f) tangential displacement along two cross-sections of the FPZ. CTOD is crack tip opening displacement and CTSD is crack tip sliding displacement.

4.2 Fracture mode estimation using strain approach

The strain approach of the 2D-DIC is based on the concept of localized strain zones formed due to an accumulation of micro-cracks inside the FPZ, which eventually coalesce, resulting in the formation of macro-crack from the notch tip. To identify the fracture mode, the evolution of minimum principal strains (ϵ_{22}; negative ($-$) strains represent tension) and maximum shear strain (γ_{max}) inside the strain localized zones were analyzed at various loading stages. Various studies (Jian-po et al., 2015; Shirole et al., 2020a) have shown that the evolutions of the minimum principal strains (ϵ_{22}) and the maximum shear strain (γ_{max}) provide a quantitative estimate of the damage due to tensile and shear micro-cracks, respectively.

Figure 6a-d presents the contours of the minimum principal strain (ϵ_{22}) and the maximum shear strain (γ_{max}) for both specimens NDB-1 and NDB-2 at the peak load stage. It is clear is from Figure 6a-d that the FPZ is formed above the notch tip in both specimens as characterized by the formation of a (narrow-band) strain localized zone. The strain concertation in the localized zone reveals higher magnitude of the principal strain (ϵ_{22}) compared to the maximum shear strain (γ_{max}) (Figure 6a-d). For instance, the strain localized zone around the notch tip in both specimens had a large concentration of tensile strain with the minimum principal strain ($\epsilon_{22} \sim -4\ to\ -3.5\%$) being 5 times the maximum shear strain (γ_{max} $\sim 0.6 - 0.8\%$) (marked points by P1 and P2 in Figure 6a-d) at the peak load stage. This suggests that the FPZ is primarily comprised of the tensile micro-cracks or mode I component. A small amount of maximum shear strain (γ_{max}) also indicates some shear micro-cracking which can be attributed to their random orientation, making them more susceptible to shear than tensile failure. This observation is consistent with other studies (Backers et al., 2005; Li and Einstein, 2017; Nasseri et al., 2006) that found some shear micro-cracking around notch tip in various rock such as Barre granite and Lac du Bonnet granite even under pure mode I loading.

To characterize the mode of fracture in a consistent manner, the evolution of minimum principal strain (ϵ_{22}) and maximum shear strain (γ_{max}) at the notch tip (marked points by P1 and P2 in Figure 6a-d) was analyzed at various loading stages for both specimens. Figure 6e-f presents the evolution of both strains at points P1 and P2 with the normalized load-point displacement (δ_{norm}) for specimens NDB-1 and NDB-2, respectively. The load-point displacement (δ) was normalized with respect to its value at the peak load stage ($\delta_{norm} = \delta/\delta_{peak}$) for each specimen. The minimum principal strains (ϵ_{22}) at both P1 and P2 points are negative, indicating that the strains are tensile and increasing in magnitude with the increase in the applied load-point displacement (δ_{norm}). During the initial loading stages, the changes in the minimum principal strains (ϵ_{22}) at both points were very small (~ -0.3 to -0.1 %), which clearly suggests elastic deformation. With further loading, the magnitude of the minimum principal strain (ϵ_{22}) at both P1 and P2 points increased with an accelerated rate, signifying the initiation of the FPZ at the notch tip in both specimens. This observation is consistent with the study by Aliabadian et al. (2019) that characterized the FPZ initiation with significant strain accumulation in the strain localized zone. As compared to minimum principal strain (ϵ_{22}), the maximum shear strain (γ_{max}) at both P1 and P2 points was negligible (< 0.2%) during the majority of the experiment. While maximum shear strain (γ_{max}) increased near the peak load stage, its magnitude in both specimens (γ_{max}) was significantly lower as compared to the minimum principal strain (ϵ_{22}). Therefore, it can be concluded that FPZ transition to mode I fracture in both specimens based on the strain approach of 2D-DIC.

4.3 Characterization of the FPZ evolution using 2D-DIC analysis

This section presents the characterization of the FPZ evolution based on a consistent methodology developed by authors (for details, see Garg et al., 2020a-b). This methodology used the concept of the cohesive zone model (CZM) to identify the transitions among the three stages of the FPZ evolution, namely (a) the elastic deformation, (b) the FPZ initiation and its propagation, and (c) the macro-crack initiation that leads to unstable crack propagation. According to the CZM, the tip of the FPZ (i.e., the boundary between the elastic zone and the FPZ) is represented by elastic opening (w_e) and sliding displacements (γ_e) for pure mode I and pure mode II cracks, respectively (Xie et al., 2017). Similarly, the tip of the macro-crack (the boundary between the FPZ and macro-crack) is represented by the critical opening (w_c) and sliding displacement (γ_c) for pure mode I and pure mode II cracks, respectively (Xie et al., 2017). In our earlier study (Garg et al., 2020b), both elastic (w_e) and critical displacements (w_c) were estimated based on the evolution of crack opening displacement at the notch tip ($CTOD$) which account for the FPZ evolution of mode I component. A similar approach can be applied for characterizing the FPZ evolution of mode II component using an equivalent parameter such as crack tip sliding displacement ($CTSD$).

Table 2: Experimental results of Barre granite specimens under pure mode II loading.

Specimen #	NDB-1	NDB-2
Peak load (kN)	12.93	15.69
Elastic Opening (w_e) (μm)	11.7	3.6
FPZ initiation load (kN) (Pre-peak regime)	10.5	12.2
Critical opening (w_c) (μm)	42.3	34
Crack initiation load (kN) (Post-peak regime)	12.92	15.65

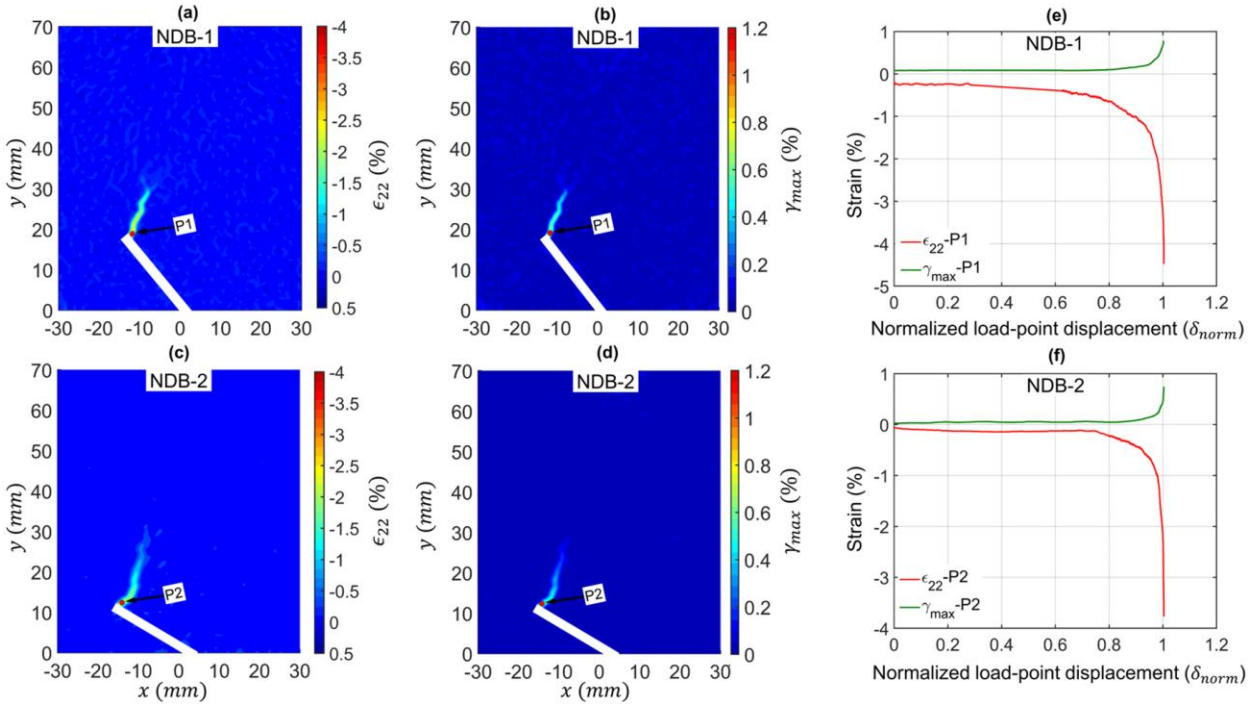

Figure 6. Contour of (a-c) minimum principal strain (ϵ_{22}) (b-d) and maximum shear strain (γ_{max}) obtained by 2D-DIC at peak load stage for two specimens NBD-1 and NDB-2 ;(e-f) Variation of minimum principal strain (ϵ_{22}) and maximum shear strain (γ_{max}) at points P1 and P2 with the load-point displacement. Positive (+) and negative (-) strains represent compression and tension, respectively.

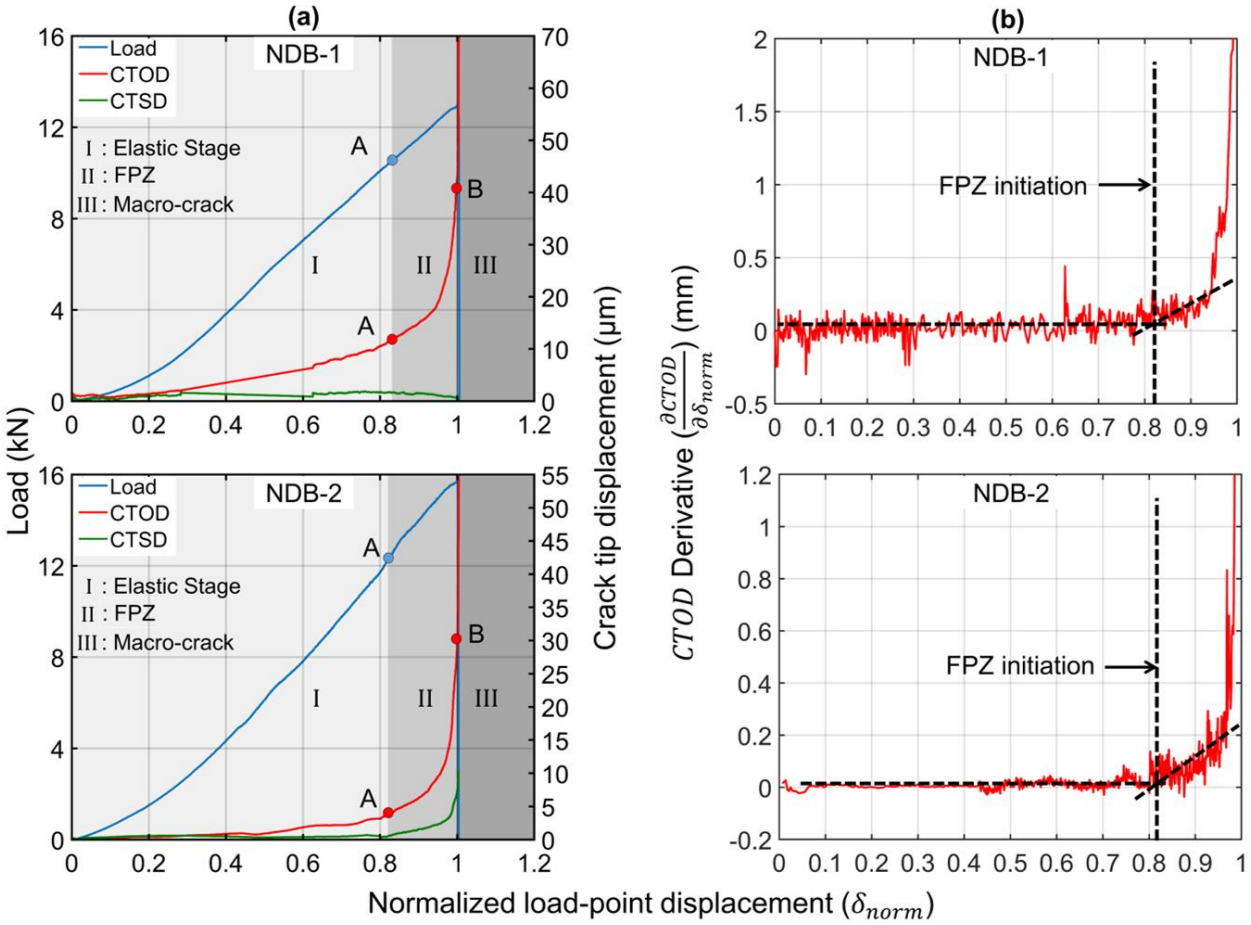

Figure 7. (a) Variation of load, $CTOD$ and $CTSD$ with the applied load-point displacement for two specimens NDB-1 and NDB-2; (b) FPZ initiation based on $CTOD$ derivative for two specimens NDB-1 and NDB-2.

As mentioned earlier (section 4.1), the $CTOD$ and $CTSD$ were calculated using normal and tangential displacements along the two cross-sections ($x_1 = \pm 2\ mm$) parallel to the FPZ as shown by Figure 5e-f for specimen NDB-1. Figure 7a shows the evolution of the $CTOD$ and $CTSD$ with the normalized load-point displacement (δ_{norm}) for both specimens NDB-1 and NDB-2. In the adopted methodology, the elastic stage is characterized by the linear variation of $CTOD$ with respect to normalized load-point displacement (δ_{norm}) as observed in both specimens NDB-1 and NDB-2 during the initial loading stages (0-82% peak load in the pre-peak regime) (Figure 7a). The FPZ initiation from the notch tip is characterized by an accelerated rate of increase in $CTOD$, resulting in its nonlinear variation with respect to normalized load-point displacement (δ_{norm}). The FPZ initiation occurred at point A and at 81% and 78% of the peak load in the pre-peak stage for specimens NDB-1 and NDB-2, respectively. The onset of non-linearity in the $CTOD$-normalized load-point displacement (δ_{norm}) curve is estimated as the point of the first significant change in the derivative of $CTOD$ with respect to the normalized load-point displacement ($\partial CTOD/\partial\delta_{norm}$) as denoted by FPZ-I in Figure 7b for specimens NDB-1 and NDB-2. The macro-crack initiation, in the adopted methodology, is marked by the point of a rapid jump in $CTOD$ with respect to a small change in the normalized load-point displacement (δ_{norm}) as shown by point 'B' (Figure 7a). The rapid jump in the $CTOD$ can be attributed to the onset of the unstable crack propagation, which is a consequence of macro-crack (traction-free crack) initiation at the notch tip. For both specimens, the elastic opening displacement (w_e) is defined as the point of non-linearity in $CTOD$ vs. load-point displacement curve, while the critical crack opening displacement (w_c) is estimated by the point of rapid jump in the $CTOD$. Table 2 presents the results of the specimens tested in this study. Interestingly, the values of both the elastic (w_e) and the critical crack opening displacement (w_c) obtained for the Barre granite specimens under pure mode II loading were similar to values obtained by authors (see Garg et al., 2020a-b) for cases of mode I loading on the same rock. This suggests that the FPZ evolution of mode I fracture doesn't change with respect to the loading conditions at the notch tip.

As a compared to $CTOD$, the $CTSD$ is negligible (< 5 μm) in both specimens except around the peak load stage in the case of specimen NDB-2 (Figure 7a). At this loading stage, the $CTSD$ of the specimen NDB-2 has reached 10 μm but is significantly lower than its $CTOD$ (~ 60 μm) (Figure 7a). A relatively larger value of $CTSD$ in the specimen NDB-2 compared to NDB-1 can be attributed to the tortuous crack path from the notch tip in the former case (Figure 5a). As mentioned earlier (section 4.1), tangential displacements in the specimen NDB-2 were calculated using the average crack path instead of the local FPZ path from the notch tip that resulted in a small amount of sliding displacement. Based on the evolution of the $CTOD$ and the $CTSD$, it can be concluded that the FPZ evolved into mode I fracture in both specimens despite the application of pure mode II loading at the notch tip.

5. CONCLUSION

The notched deep beams of Barre granite were tested under pure mode II loading conditions to characterize the development of the FPZ using the DIC imaging. In both tested NDB specimens, a kinked fracture was observed from the notch tip under pure mode II loading. The mode of fracture was determined using both displacement and strain approaches of 2D-DIC. The analysis showed that the FPZ included a large value of opening displacement and high tensile strain concentration, indicating the presence of mode I component inside the FPZ. Additionally, the sliding displacements were found to be negligible compared to opening displacements, indicating crack initiation under pure mode I. The mode II loading in both specimens only resulted in a non-symmetric normal displacements pattern around the notch. The evolution of the FPZ was characterized into three stages using the methodology developed by authors (Garg et al., 2020a-b), which analyzed the variation of crack tip opening displacements ($CTOD$) and the crack tip sliding displacements ($CTSD$) with respect to normalized beam deflection normalized load-point displacement (δ_{norm}). The results showed that the evolution of the FPZ of mode I fracture under pure mode II loading is similar to cases of pure mode I loading of the same rock. This suggests that the evolution of the FPZ of mode I fracture independent of loading condition.

ACKNOWLEDGEMENTS

Funding for this research was provided by the National Science Foundation under award number 1644326. The authors are grateful for this support.

REFERENCES

1. Aliabadian Z, Zhao GF, Russell AR. (2019). Crack development in transversely isotropic sandstone discs subjected to Brazilian tests observed using digital image correlation. International Journal of Rock Mechanics and Mining Sciences;119:211–21.
2. Aliha MRM, Ashtari R, Ayatollahi MR. (2006). Mode I and Mode II Fracture Toughness Testing for a Coarse Grain Marble. Applied Mechanics and Materials;5–6:181–8.
3. Aliha MRM, Ayatollahi MR. (2014). Rock fracture toughness study using cracked chevron notched Brazilian disc specimen under pure modes I and II

loading – A statistical approach. Theoretical and Applied Fracture Mechanics;69:17–25.

4. Ayatollahi MR, Sistaninia M. (2011). Mode II fracture study of rocks using Brazilian disk specimens. International Journal of Rock Mechanics and Mining Sciences;48:819–26.

5. Backers T, Stanchits S, Dresen G. (2005). Tensile fracture propagation and acoustic emission activity in sandstone: The effect of loading rate. International Journal of Rock Mechanics and Mining Sciences;42:1094–101.

6. Dai F, Xia K. (2010). Loading Rate Dependence of Tensile Strength Anisotropy of Barre Granite. Pure and Applied Geophysics;167:1419–32.

7. Dutler N, Nejati M, Valley B, Amann F, Molinari G. (2018). On the link between fracture toughness, tensile strength, and fracture process zone in anisotropic rocks. Engineering Fracture Mechanics;201:56–79.

8. Garg P, Shirole D, Hedayat A, Griffiths DV (2019). Coupled ultrasonic and digital imaging of crack initiation and growth in prismatic Lyon sandstone rocks. In: 53rd U.S. Rock Mechanics/Geomechanics Symposium.

9. Garg P, Shirole D, Hedayat A, Griffiths DV (2020a). Numerical simulation of fracture initiation in Barre Granite using an experimentally validated XFEM model. In: 54rd U.S. Rock Mechanics/Geomechanics Symposium.

10. Garg, P., Hedayat, A., and Griffiths, D.V. (2020b). Characterization of fracture process zone using surface deformation and strain field in brittle rocks. Rock Mechanics and Rock Engineering (under review).

11. Ghamgosar M, Erarslan N. (2016). Experimental and Numerical Studies on Development of Fracture Process Zone (FPZ) in Rocks under Cyclic and Static Loadings. Rock Mechanics and Rock Engineering;49:893–908.

12. Goldsmith W, Sackman JL, Ewerts C. (1976). Static and dynamic fracture strength of Barre granite. International Journal of Rock Mechanics and Mining Sciences & Geomechanics Abstracts;13:303–9..

13. Hedayat A, Pyrak-Nolte LJ, Bobet A. (2014). Multi-Modal Monitoring of Slip Along Frictional Discontinuities. Rock Mechanics and Rock Engineering;47:1575–87.

14. Iqbal MJ, Mohanty B. (2006). Experimental Calibration of ISRM Suggested Fracture Toughness Measurement Techniques in Selected Brittle Rocks. Rock Mechanics and Rock Engineering;40:453.

15. Ji WW, Pan PZ, Lin Q, Feng XT, Du MP. (2016). Do disk-type specimens generate a mode II fracture without confinement? International Journal of Rock Mechanics and Mining Sciences;87:48–54.

16. Jian-po L, Yuan-hui L, Shi-da X, Shuai X, Chang-yu J. (2015). Cracking mechanisms in granite rocks subjected to uniaxial compression by moment tensor analysis of acoustic emission. Theoretical and Applied Fracture Mechanics;75:151–9.

17. Labuz JF, Shah SP, Dowding CH. (1987). The fracture process zone in granite: evidence and effect. International Journal of Rock Mechanics and Mining Sciences & Geomechanics Abstracts;24:235–46.

18. Li BQ, Einstein HH. (2017). Comparison of Visual and Acoustic Emission Observations in a Four Point Bending Experiment on Barre Granite. Rock Mechanics and Rock Engineering;50:2277–96.

19. Lin Q, Ji WW, Pan PZ, Wang S, Lu Y. (2019). Comments on the mode II fracture from disk-type specimens for rock-type materials. Engineering Fracture Mechanics;211:303–20.

20. Lin Q, Wang S, Pan PZ, Ji WW, Lu Y. (2020). Fracture initiation under pure shear revisited: Remarks on the mode II fracture in quasi-brittle materials. Theoretical and Applied Fracture Mechanics;109.

21. Liu HZ, Lin JS, He J da, Xie HQ. (2018). Dominant mode of planar fractures and the role of material properties. Engineering Fracture Mechanics;195:57–79.

22. Lu Y, Li W, Wang L, Meng X, Wang B, Zhang K. (2019). In-situ microscale visualization experiments on microcracking and microdeformation behaviour around a pre-crack tip in a three-point bending sandstone. International Journal of Rock Mechanics and Mining Sciences;114:175–85.

23. Luo Y, Ren L, Xie LZ, Ai T, He B. (2017). Fracture Behavior Investigation of a Typical Sandstone Under Mixed-Mode I/II Loading Using the Notched Deep Beam Bending Method. Rock Mechanics and Rock Engineering;50:1987–2005.

24. Miao S, Pan PZ, Yu P, Zhao S, Shao C. (2020). Fracture analysis of Beishan granite after high-temperature treatment using digital image correlation. Engineering Fracture Mechanics;225.

25. Mirsayar MM, Razmi A, Aliha MRM, Berto F. (2018). EMTSN criterion for evaluating mixed mode I/II crack propagation in rock materials. Engineering Fracture Mechanics;190:186–97.

26. Moazzami M, Ayatollahi MR, Akhavan-Safar A. (2020). Assessment of the fracture process zone in

rocks using digital image correlation technique: The role of mode-mixity, size, geometry and material. International Journal of Damage Mechanics;29:646–66.

27. Nasseri MHB, Grasselli G, Mohanty B. (2010). Fracture Toughness and Fracture Roughness in Anisotropic Granitic Rocks. Rock Mechanics and Rock Engineering;43:403–15.
28. Nasseri MHB, Mohanty B, Young RP. (2006). Fracture Toughness Measurements and Acoustic Emission Activity in Brittle Rocks. Pure and Applied Geophysics;163:917–45.
29. Saadat M, Taheri A. (2019). Modelling Micro-cracking Behaviour of Pre-cracked Granite Using Grain-Based Distinct Element Model. Rock Mechanics and Rock Engineering;52:4669–92. https://doi.org/10.1007/s00603-019-01862-0.
30. Sharafisafa M, Shen L, Xu Q. (2018). Characterisation of mechanical behaviour of 3D printed rock-like material with digital image correlation. International Journal of Rock Mechanics and Mining Sciences;112:122–38.
31. Shirole D, Hedayat A, Walton G. (2020a). Illumination of Damage in Intact Rocks by Ultrasonic Transmission-Reflection and Digital Image Correlation. Journal of Geophysical Research: Solid Earth;125.
32. Shirole D, Walton G, Hedayat A. (2020b). Experimental investigation of multi-scale strain-field heterogeneity in rocks. International Journal of Rock Mechanics and Mining Sciences;127.
33. Sutton, M. A., Orteu, J., and Schreier, H. W. (2009). Image correlation for shape, motion and deformation measurements. New York: Springer.
34. Xie Y, Cao P, Jin J, Wang M. (2017). Mixed mode fracture analysis of semi-circular bend (SCB) specimen: A numerical study based on extended finite element method. Computers and Geotechnics;82:157–72.
35. Xing Y, Huang B, Ning E, Zhao L, Jin F. (2020). Quasi-static loading rate effects on fracture process zone development of mixed-mode (I-II) fractures in rock-like materials. Engineering Fracture Mechanics;240:107365
36. Zhang G, Xing Y, Wang L. (2018). Comprehensive sandstone fracturing characterization: Integration of fiber Bragg grating, digital imaging correlation and acoustic emission measurements. Engineering Geology;246:45–56.